



 Cite this: *RSC Adv.*, 2021, 11, 13653

# Design of new bioinspired GO-COOH decorated alginate/gelatin hybrid scaffolds with nanofibrous architecture: structural, mechanical and biological investigations

 Jana Ghitman,<sup>a</sup> Elena Iuliana Biru,<sup>a</sup> Elena Cojocaru,<sup>a</sup> Gratiela Gradisteanu Pircalabioru,<sup>bc</sup> Eugeniu Vasile<sup>d</sup> and Horia Iovu \*<sup>ae</sup>

The current research study deals with the design and investigation of novel bioinspired and biocompatible GO-COOH decorated hybrid polymeric scaffolds with nanofibrous architecture as biomaterials with highly appropriate features for functional restoration of damaged tissue. Gelatin and alginate, two biobased-polymers with excellent biocompatibility, high microenvironment biomimicry and ability for proper guidance of cell development in combination with carboxylated graphene oxide (GO-COOH), embody the matrix of electrospun hybrid scaffolds. The underlying principle is based on various types of interactions that can take place between the functionalities of the system's entities (proved by DLS) and their synergy in improving the structural integrity, mechanical tailorability and biological performances of the new nanofibrous GO-COOH decorated hybrid scaffolds. The nanofibrous structure along with the presence of GO-COOH are established by SEM. The new covalent bonds formed between various functionalities of the protein-polysaccharide-GO-COOH system are proved by FTIR and XPS. The physico-chemical state of GO-COOH lattices within the hybrid structures is investigated by Raman spectrometry. The interpenetrated network of bicomponent structures determines a 10-fold increase of Young's modulus as compared to monocomponent counterparts while the dispersion of GO-COOH significantly increases the elasticity of materials. The biological results (MTT and LDH assays) indicate a good cytocompatibility of crosslinked bicomponent AGS scaffolds; the metabolic cellular activity is substantially improved following the GO-COOH addition, suggesting that GO-COOH can support the cell adhesion, growth and proliferation.

 Received 22nd February 2021  
 Accepted 26th March 2021

DOI: 10.1039/d1ra01432c

[rsc.li/rsc-advances](http://rsc.li/rsc-advances)

## 1. Introduction

So far, the repair and regeneration of damaged tissues is a subject of substantial interest within the biomedical community, representing one of the most challenging tasks for clinical therapy. Among the complexity of materials used in both academia and clinical research, rationally designed bioinspired scaffolds that, beside physical support provided for cells, can mimic the structure and biological functions of the extracellular matrix (ECM) and are able to advance the regeneration of pathologically altered tissue architecture represent

a thriving strategy in biomedicine.<sup>1</sup> Mainly, the bioinspired polymer-based scaffolds with nanofibrous architecture owing to their biomimetic microenvironments (potential ability to mimic ECM), appropriate guidance and mechanical support for cell adhesion and proliferation until hosts cells can repopulate and resynthesize a new natural matrix, are lately of particular importance to tissue engineering and regenerative medicine (TERM).<sup>2,3</sup> This design combines the features of nanofibrous structure: extreme large specific area, controllable mechanical properties and highly interconnected porosity<sup>4,5</sup> with the valuable characteristics of bio-based polymers *e.g.*, biocompatibility, biomimetic properties, hydrophilicity, non-toxicity, and less-immunogenicity, ability to promote cellular attachment, proliferation and formation of the new tissue in three-dimensions.<sup>6,7</sup> Beyond the above-mentioned advantages, these biomaterials are highly profuse in nature, while the versatility in crosslinking and functionalization represent warranted ways to overcome the shortcoming associated with their insufficient mechanical properties.<sup>6-8</sup> Likewise, the global mechanical properties of these biomaterials can be modulated, by varying

<sup>a</sup>Advanced Polymer Materials Group, University Politehnica of Bucharest, 1-7 Gh Polizu Street, 011061 Bucharest, Romania. E-mail: [horia.iovu@upb.ro](mailto:horia.iovu@upb.ro)

<sup>b</sup>Microbiology Immunology Department, Faculty of Biology, University of Bucharest, 050095 Bucharest, Romania

<sup>c</sup>Research Institute of the University of Bucharest, 050095 Bucharest, Romania

<sup>d</sup>Department of Oxide Materials Science and Engineering, University Politehnica of Bucharest, 1-7 Gh. Polizu, 060042 Bucharest, Romania

<sup>e</sup>Academy of Romanian Scientists, 54 Splaiul Independentei Street, 050094 Bucharest, Romania



the type and amount of the crosslinking or functionalization agent, prospecting the design of a biomaterial with highly suitable physico-mechanical, eco-friendly and biodegradable performances for a particular application in modern personalized biomedicine.<sup>9,10</sup> Numerous research studies have confirmed that the nanoscale construction of biomaterial scaffolds is more appropriate for cells adhesion and proliferation, providing a superior structural support for developing new tissue as compared to microscale counterparts.<sup>2,10,11</sup> In the frame of the current challenges, the electrospinning technique remains a straightforward, versatile, and irreplaceable method for the fabrication of nanofibrous structures with highly proper biomimetic, mechanical and biological features for TERM.<sup>13,14</sup> Besides, the ability to generate biomaterials from bio-based polymers remains an obvious and prospective approach that can provide practically unlimited resources for the development of biocompatible and biomimetic scaffolds used in functional restoration of damaged tissue.<sup>2,15,16</sup>

Alginate is a seaweed-derived anionic heteropolysaccharide with linear unbranched chains, which consist of two randomly arranged C5-epimers,  $\alpha$ -L-guluronate (G unit) and  $\beta$ -D-mannuronate (M unit) in various proportions.<sup>15,17</sup> Considering that the main components of ECM are proteoglycans, glycosaminoglycans and fibrous proteins, the importance of alginate in TERM is owed not only to its unique biocompatibility and biodegradability but also to its structural resemblance to ECM's glycosaminoglycan.<sup>2</sup> Studies have shown that alginate-based scaffolds can proffer a suitable environment for chondrocytes proliferation withal maintaining their functional phenotype by producing the cartilage-like ECM.<sup>18,19</sup> However, the fabrication of electrospun alginate-based scaffolds is one of the biggest challenges, because of polysaccharide inability to form in water a sufficient number of chain entanglements to promote the fiber formation, also the polyelectrolyte character of alginate hinders its electrospinning capacity. One way to solve this problem is to blend the alginate with a supporting polymer *e.g.*, polyethylene oxide (PEO) that can interact with polysaccharide chains through hydrogen bonding, increasing thus its spinnability properties.<sup>2,14,17</sup>

Gelatin is one of the most studied and exploited biopolymers in TERM owing to its excellent biomimetic, biological properties and versatility in formulation.<sup>6,20</sup> Studies have shown that the RGD (the tripeptide Arg-Gly-Asp) binding motif from its primary structure acts as a recognition sequence for integrin-mediated cells adhesion, which improves substantially the spreading and proliferation of cells on gelatin-based biomaterials.<sup>20,21</sup> Unlike alginate, gelatin presents remarkable spinnability, regardless the type of fibrous scaffold (*e.g.*, simple, hybrid or composite) and electrospinning method (*e.g.*, electrospinning, co-electrospinning, wet electrospinning).<sup>10,22,23</sup>

Graphene, "the mother of all graphitic form of carbon"<sup>24</sup> represents a single layer of carbon atoms held together in a two-dimensional lattice by a backbone of overlapping  $sp^2$  hybrids bonds.<sup>13</sup> Graphene oxide (GO) and carboxylated graphene oxide (GO-COOH) represent graphene derivatives with obviously higher hydrophilicity and chemical activity, originated from the presence of oxygen functionalities and defects<sup>13</sup> which are

frequently selected over graphene in various biomedical fields.<sup>25</sup> The dispersion of GO/GO-COOH into the natural polymers-based biomaterials represents an appropriate strategy in designing bioinspired hybrid or composite scaffolds that can better suit the mechanical and physiological demands of host tissue.<sup>24,25</sup>

Fibrous scaffolds based on gelatin, alginate/PEO, gelatin/GO or alginate/GO designed by different electrospinning techniques are trending topics in the specialized literature.<sup>18–23,26,27</sup> Conversely, the literature presents only few very recent papers that approach the electrospinning method to engineer gelatin-alginate composite membrane<sup>28</sup> or hydrogel<sup>29</sup> with nanofibrous architecture, presenting the experimental results of these materials and their potential biomedical use. Besides, the concept of combining two bio-based polymers (alginate and gelatin) with GO-COOH and electrospinning technique to engineer hybrid scaffolds with nanofibrous architecture and proper characteristics for TERM, has not been approached yet in the specialized literature.

Herein, we report the development of novel bicomponent hybrid scaffolds based on natural polymers (alginate and gelatin) and GO-COOH with nanofibrous architecture using electrospinning approach, along with the investigation of the morphological (SEM), structural (FTIR, Raman, XPS), nano-mechanical (Nanoindentation) and biological features in correlation with the possibility to be considered potent bioinspired materials for tissue regeneration. The underlying principle consists in combining the excellent features of each component into one entity and designing the bioinspired GO-COOH-decorated hybrid nanofibrous scaffolds with highly appropriate features that might ensure both mechanical and biological support for cells, advancing thus the regeneration of damaged tissue; furthermore, could open new research directions in TERM.

## 2. Experimental

### 2.1 Materials

Gelatin from cold water fish skin (Gel) was purchased from Sigma-Aldrich Chemie GmbH (Germany). Sodium Alginate from brown algae (Alg), Polyethylene oxide with  $M_w = 600$  KDa (PEO), 4-(1,1,3,3-tetramethylbutyl) phenyl-polyethylene glycol (Triton-X 100), glutaraldehyde Grade I, 50% solution in water (GA) and  $CaCl_2$  were supplied from Sigma-Aldrich Chemie GmbH, Germany; carboxylated graphene oxide (GO-COOH) was provided by NanoInnova Technology. All materials were used as received and all the experiments were performed using ultra-pure water from Milli-Q Plus system (Millipore Corporation).

### 2.2 Preparing the precursor mixtures to engineer GO-COOH-decorated hybrid mono/bicomponent scaffolds based on natural polymers with nanofibrous architecture

Initially, to design nanofibrous scaffolds based on gelatin (GS), sodium alginate (AS) or bicomponent scaffolds based on sodium alginate/gelatin (AGS), three different polymer solutions, consisting from gelatin (40 wt% of gelatin was dissolved

Table 1 The detailed composition of all electrospun scaffolds

Sample	The sample compositions			
	Precursor system (mL)	Alg/PEO/Gel ratio (v/v/v)	wt% GO-COOH	wt% Triton-X
GS	5	0/0/5	—	0.5
HGS-0.1	5	0/0/5	0.1	0.5
HGS-0.2	5	0/0/5	0.2	0.5
AS	5	3.5/1.5/0	—	0.5
HAS-0.1	5	3.5/1.5/0	0.1	0.5
HAS-0.2	5	3.5/1.5/0	0.2	0.5
AGS	5	2/1/2	—	0.5
HAGS-0.1	5	2/1/2	0.1	0.5
HAGS-0.2	5	2/1/2	0.2	0.5

in ultrapure water with 0.5 wt% Triton-X 100 at 40 °C for 12 hours), sodium alginate (containing 4 wt% sodium alginate and 4 wt% PEO dissolved in aqueous solution of 0.5 wt% Triton-X 100 at 60 °C for 1 day, the ration between Alg/PEO was 7/3 (v/v)) and sodium alginate/gelatin (the solution consisting from Alg, PEO and Gel in a ratio of 2/1/2 (v/v/v) dissolved in 0.5 wt% Triton-X aqueous solution) were prepared and subjected to electrospinning process.

The precursor mixtures of GO-COOH-decorated hybrid scaffolds based on Gel (HGS), Alg (HAS) or Alg/Gel (HAGS) using two GO-COOH concentrations, were prepared by the surfactant addition method to improve the dispersibility of carbon-based materials reported by Dror and colleagues<sup>30</sup> with some modifications. The specific amount of GO-COOH (according to Table 1) was dispersed in an aqueous solution of 0.5 wt% Triton-X 100 and subjected to ultrasonication (Vibra-Cell CVX 130, 20 kHz, 220 V, USA) for 1 hour. Then, to the obtained mixtures the required amount of Gel (40 wt%) was added to prepare the HGS blends. To formulate the hybrid bicomponent HAGS precursor mixtures, firstly PEO (4 wt%) was dissolved in GO-COOH aqueous dispersions which were subsequently mixed with 4wt% sodium alginate solution and 40 wt% gelatin solution. The HAS blends were prepared following the same protocol except the addition of gelatin solution. The precursor mixtures were maintained under magnetic stirring at 40 °C–60 °C, until total homogenization and polymer dissolution. The detailed composition of electrospun scaffolds based on natural polymers (GS, AS, AGS) or natural polymers-based hybrid scaffolds decorated with GO-COOH (HGS, HAS, HAGS) in different concentrations are presented in Table 1.

### 2.3 Electrospinning process

The previously reported blend electrospinning method<sup>12,31</sup> was applied to obtain scaffolds based on natural polymers or GO-COOH-decorated hybrid scaffolds. The electrospinning process was performed using a climate-controlled electrospinning equipment (IME Technologies, Netherlands). The precursor mixtures were pumped through a syringe with G 22 needle with the rate of 5  $\mu\text{L min}^{-1}$ . The distance between the needle tip and the collector plate (covered with aluminum foil)

was fixed at 16 cm. During the electrospinning process the power supply voltage was adjusted in the range of 15 kV to 22 kV, to ensure the formation of the Taylor cone as well to avoid the spraying process. The temperature and relative humidity within the electrospinning chamber were set at 25 °C respectively 35–40%. The electrospun nanofibers were dried in the oven at 37 °C for 24 h.

The crosslinking step of the electrospun Gel-based scaffolds (GS, HGS-0.1 and HGS-0.2) was carried out in vapor of aqueous GTA solution (50% w/v), according to previous reported method,<sup>23</sup> obtaining GS', HGS'-0.1 and HGS'-0.2. Briefly, the dried electrospun Gel-based scaffolds were placed on a holder and were suspended in a sealed chamber. The aqueous GTA solution was placed under the samples and the Gel-based scaffolds were crosslinked in GTA vapor for 48 h at room temperature. The ionic gelation of electrospun AS or Alg-based hybrid scaffolds decorated with GO-COOH was done by immersing the samples in absolute ethanol with 2 wt%  $\text{CaCl}_2$  for 2 h,<sup>32</sup> resulting AS', HAS'-0.1, HAS'-0.2 scaffolds. Regarding to the bicomponent AGS and GO-COOH decorated HAGS, the two-step crosslinking process was employed, generating the crosslinked scaffolds with interpenetrated hybrid network (AGS', HAGS'-0.1, HAGS'-0.2 respectively). Initially the samples were suspended in vapor of aqueous GTA solution (50% w/v) to crosslink the protein, then the polysaccharide ionic gelation in a 2 wt%  $\text{CaCl}_2$  absolute ethanolic solution was done.

### 2.4 Characterization techniques

**Dynamic light scattering (DLS).** The hydrodynamic diameter ( $d$ ), diffusion coefficient ( $D$ ), polydispersity (PDI) and zeta potential ( $\zeta$ ) measurements were achieved by Dynamic Light Scattering (Zetasizer Nano ZS, Malvern Instrument, UK) device, equipped with a He/Ne laser. Size measurements were performed at a scattering angle of 173° while the electrophoretic mobility investigations (converted in zeta potentials with the Helmholtz–Smoluchowski equation) were carried out at one of 13°. Aqueous samples with 0.1 wt% concentrations were prepared and subjected to DLS measurements using plastic capillary cells with electrodes at each end (Malvern Instruments). The samples were equilibrated for 120 s at 25 °C in the instrument, then for each specimen 15 successive cycles were run, the results were done in triplicate and the data were presented as mean  $\pm$  SD.

**Scanning electron microscopy (SEM).** SEM investigations were carried out on a Quanta Inspect F50 (USA), equipped with a field-emission electron beam gun (FEG) with 1.2 nm resolution. The electrospun scaffolds were sputter-coated with a thin gold layer and their morphology was observed by the means of field emission gun operated at 30 kV.

**FTIR spectrometry.** FTIR measurements were done on a Vertex 70 Bruker FTIR spectrometer (USA), equipped with an attenuated total reflectance (ATR) accessory. For each sample 32 scans were registered in the ATR-FTIR mode, at room temperature and a resolution of 4  $\text{cm}^{-1}$  in 600–4000  $\text{cm}^{-1}$  wavenumber region.

**Raman spectrometry.** The Raman spectra were collected using a Renishaw in Via Raman microscope system (473 nm laser excitation, Renishaw), equipped with a 100× objective at a 0.4 mW incident power. The spectra were collected in the region  $\sim 1000\text{--}3200\text{ cm}^{-1}$  to encompass the contributions from both 1st and 2nd order scattering.

**XPS spectroscopy.** The X-ray photoelectron spectroscopy (XPS) measurements were recorded on a Thermo Scientific K-Alpha instrument (Vietnam), equipped with an aluminum anode monochromatic source (1486.6 eV) at a pressure of  $2 \times 10^{-9}$  mbar. The binding energy was calibrated by placing the C 1s peak at 284.8 eV as internal standard. Charging effects were compensated by a flood gun and the XPS spectra were collected after the subtraction of Smart background.

**Contact angle.** The wetting properties of all electrospun crosslinked scaffolds were investigated by Kruss DSA100S instrument (Germany), equipped with a CF03 digital camera. The contact angle was measured 10 seconds after deposition of the droplet using the sessile drop method. At least 3 measurements were done in different locations on the sample at room temperature. The results were reported using the Young Laplace equation and represent the averaged values.

**Nanoindentation.** The nanomechanical properties (Hardness ( $H$ ), Stiffness ( $S$ ) and Young's modulus ( $E$ )) of all electrospun crosslinked mono/bicomponent or GO-COOH decorated hybrid scaffolds were investigated using a Nanoindenter G200 instrument (Agilent Technologies, USA). The samples were fixed on the sample holder for the Standard stage and the indentations were performed using the Berkovich diamond tip with a 20 nm radius. The Express Test to a Displacement method from the NanoSuit software was used, performing for each sample 400 indents at 50  $\mu\text{m}$  distance from each other and 500 nm displacement into the surface and the poisson ratio of 0.4. The results calculated for each nanomechanical parameter represent the averaged values over all valid indents performed for each sample.

## 2.5 Biocompatibility studies

In this study, NCTC fibroblasts (American Type Culture Collection, USA) were used to investigate the biocompatibility, proliferation and cytotoxic potential of all crosslinked nanofibrous mono/bicomponent and GO-COOH decorated hybrid scaffolds. Briefly,  $5 \times 10^5$  cells were seeded in 24-well plates containing DMEM supplemented with 10% FBS and 1% penicillin-streptomycin. Afterwards, cells suspension was distributed over the scaffolds and the resulting specimens were maintained in standard culture conditions (37 °C, humidified atmosphere of 95% air and 5% CO<sub>2</sub>) for up to 6 days. Cell viability and proliferation potential were evaluated by 3-[4,5-dimethylthiazole-2-yl]-2,5-diphenyltetrazolium bromide (MTT) metabolic assay, after 2 and 6 days of culture. This assay is based on the activity of mitochondrial dehydrogenases of viable cells to reduce the MTT to purple formazan crystals. The specimens were incubated with 1 mg mL<sup>-1</sup> MTT solution for 4 hours at 37 °C in the same atmosphere and the absorbance at 550 nm was measured by Flex Station 3 spectrophotometer. Regarding

to the LDH assay, the resulted culture media were mixed with the components of the Tox-7-KT kit, according to the manufacturer's instructions and incubated in the dark for 20 min, followed by spectrophotometric measurement at 490 nm. The culture of cells without scaffolds was used as control. All tests were done in triplicate and the statistical analysis was performed by one-way ANOVA test, considering statistical significance if  $p < 0.05$ .

## 3. Results and discussion

### 3.1 Investigation of the interactions between the system components

Among the key factors that drive the integrity, stability and global performances of the designed nanofibrous scaffolds as potent biomaterials are the various interactions that can take place between the components of the system. Hence, based on their specific or collective diffusivity ( $D$ ), the individual or global behaviour of the species from a system can be investigated by monitoring the hydrodynamic features and electrophoretic mobility of molecular entities involved in that system. The collected hydrodynamic parameters are presented in Table 2.

A high discrepancy between the hydrodynamic characteristics of each individually investigated component, mainly originated from their chemistry, can be observed. The mean hydrodynamic size ( $d$ , nm) of a species refers to an equivalent sphere diameter drawn around the analysed molecules with the same diffusion behaviour.<sup>33</sup> Zeta potential ( $\zeta$ , mV) implies the electrical properties of an entity at slipping plan, being an indicator of the surface charges and a proper index of the interaction magnitude between various colloidal species.<sup>34</sup> The positive zeta potential of Gel is originated from the protonated amino groups of arginine, glutamic and aspartic acids, which are in a high level in the chemical composition, a particularity of fish gelatin.<sup>35</sup> At the same time, the negative electrokinetic potential of polysaccharide, carboxylated graphene oxide and polyether is attributed to their carboxylic and hydroxylic functionalities, respectively hydroxylic end-groups from the PEO backbones.

In the case of multicomponent systems, it appears that a combination of processes *e.g.*, hydrophobic interactions,

Table 2 The hydrodynamic characteristics of raw materials and precursor systems

Sample <sup>a</sup>	$d$ (nm)	PdI	$\zeta$ (mV)	$D$ ( $\mu^2\text{ s}^{-1}$ )
Gel	247.8 $\pm$ 0.56	0.35 $\pm$ 0.01	+8.27 $\pm$ 0.63	1.99 $\pm$ 0.02
Alg	384.60 $\pm$ 13.27	0.43 $\pm$ 0.11	-60.10 $\pm$ 0.46	1.27 $\pm$ 0.03
PEO	67.78 $\pm$ 0.27	0.60 $\pm$ 0.03	-7.65 $\pm$ 0.95	7.27 $\pm$ 0.08
GO-COOH	383.40 $\pm$ 12.61	0.47 $\pm$ 0.03	-40.00 $\pm$ 1.15	1.25 $\pm$ 0.01
AS	202.60 $\pm$ 6.10	0.62 $\pm$ 0.09	-45.70 $\pm$ 2.30	2.30 $\pm$ 0.06
HGS-0.2	2091.00 $\pm$ 30.41	0.55 $\pm$ 0.08	-2.53 $\pm$ 0.31	0.23 $\pm$ 0.08
HAS-0.2	777.60 $\pm$ 11.50	0.57 $\pm$ 0.11	-16.30 $\pm$ 0.71	0.57 $\pm$ 0.01
AGS	256.80 $\pm$ 33.23	0.72 $\pm$ 0.10	-21.90 $\pm$ 0.83	1.68 $\pm$ 0.03
HAGS-0.2	564.00 $\pm$ 47.23	0.61 $\pm$ 0.01	-33.70 $\pm$ 0.30	0.82 $\pm$ 0.03

<sup>a</sup> The samples were prepared according to the synthesis protocol.

dispersion forces (van der Waals) and hydrogen bonding effects<sup>36</sup> that take place between the involved species, lead to their conformational modification, impacting the translational diffusion coefficients and the collective hydrodynamic features. The diffusion coefficient of a colloid is directly proportional to the velocity and inversely proportional to its diameter and friction constant.<sup>37</sup> Therefore, a lowering trend of individual or collective diffusivity parameter with the increase of agglomerates size, can be observed. The HGS-0.2 system is characterized by the poorest diffusivity ( $D = 0.23 \pm 0.08 \mu^2 \text{ s}^{-1}$ ) and lowest stability ( $\zeta = -2.53 \pm 0.31 \text{ mV}$ ). A substantial improvement in stability of HGS-0.2 system ( $\zeta = -33.70 \pm 0.30 \text{ mV}$ ) followed the polysaccharide addition, is noted. The registered more than 10-folds higher  $\zeta$  value of HGS-0.2 as compared to HGS-0.2 sample and twice less when compared to pristine alginate ( $\zeta = -60.10 \pm 0.46 \text{ mV}$ ) suggests the occurrence of numerous intermolecular H-bonds between polysaccharide and protein functionalities, mainly COOH and  $\text{NH}_2$ .

Similar behaviour of natural polymers with long chains, especially protein in the presence of various molecule/media is widely reported in the literature.<sup>38,39</sup>

### 3.2 Morphology of the mono/bicomponent and GO-COOH decorated hybrid scaffolds with nanofibrous architecture

SEM micrographs reveal nanofibers with consistent beads-free and uniform morphology that is obtained by properly investigating and adjusting the solution and spinning parameters for each type of the designed scaffold (Fig. 1).

Monocomponent gelatin-based scaffolds (GS) present in SEM uniform, smooth, and well-defined fibrous structures without any defects. Then, regular, continuous nanofibrous architectures with GO-COOH sheets uniformly distributed along the nanofibers with no residual agglomerates of graphene on the outer surface are highlighted in SEM micrographs of hybrid HGS-0.1 and HGS-0.2 scaffolds. A well-defined smooth nanofibrous structure with a trivial tendency to beads formation can be observed in the micrographs of electrospun monocomponent AS scaffolds, when compared to gelatin-based

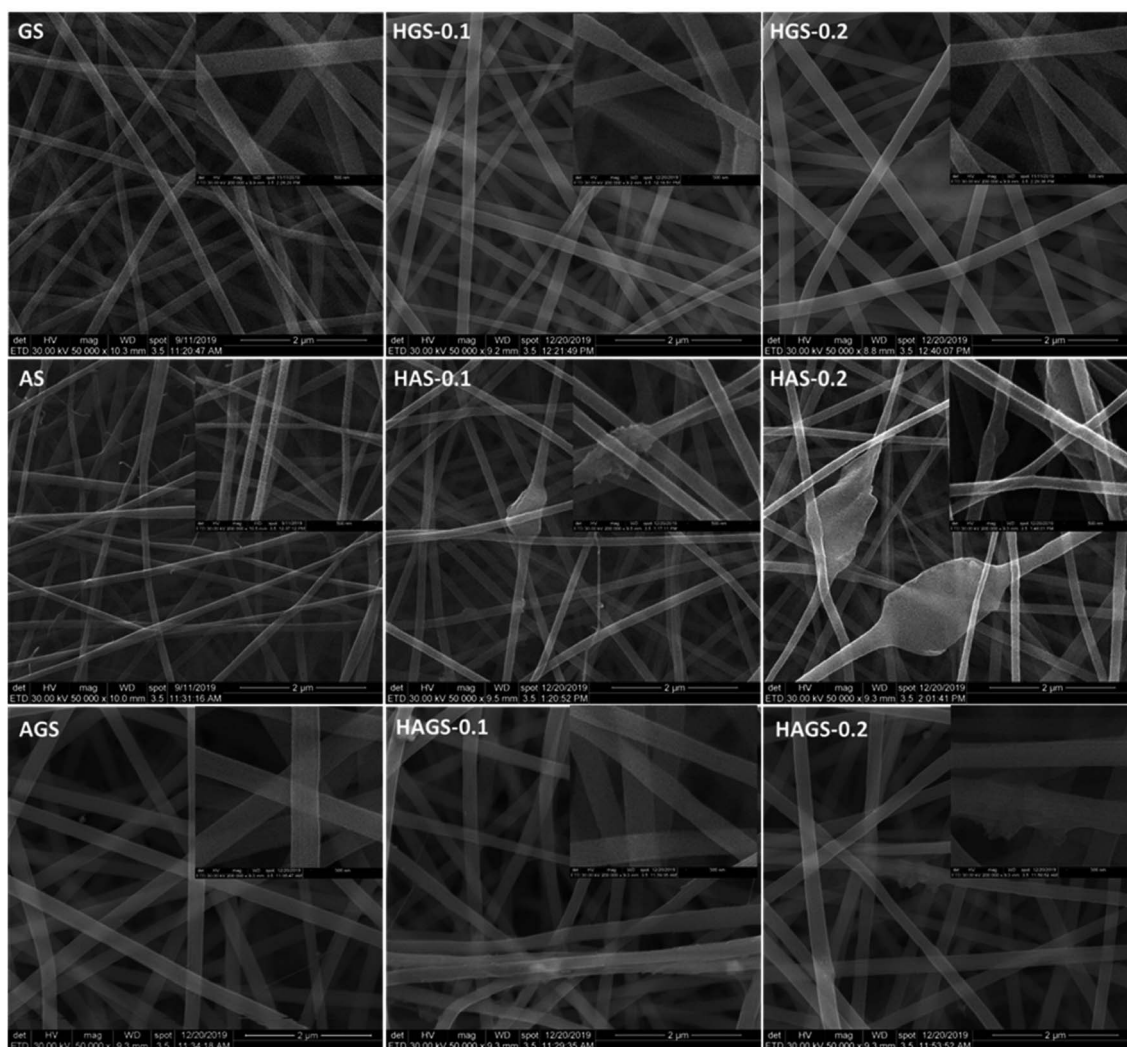


Fig. 1 SEM micrographs of all electrospun mono/bicomponent and GO-COOH decorated hybrid scaffolds with nanofibrous architecture.

counterparts (Fig. 1). Considering that sodium alginate is one of the most challenging electrospun polymers, blending the polysaccharide solution with the “carrier” PEO represents a feasible strategy in overcoming this drawback. It was concluded that as the molecular weight of PEO employed is higher, the more uniform and without defects will be the obtained nanofibers, owing to PEO–PEO interactions that will produce a sufficient chain entanglement to “carry” the polyanion from solution during the electrospinning.<sup>12,40</sup> In this study we have used a PEO with 600 kDa, with a Alg/PEO ratio of 7/3 (v/v), which might not be sufficient to ensure the optimal chain entanglements and to reduce the surface tension of precursor solution, thus explaining the slight tendency of AS nanofibers to beads formation.

The addition of GO-COOH leads to an increase in charge relaxation time and conductivity of precursor solution,<sup>41</sup> determining a visible improvement of both electrospinning and morphological features of hybrid nanofibrous structure. Uniform, beads-free hybrid HAS-0.1, HAS-0.2 nanofibers with fine dispersion of the GO-COOH sheets along them, without forming detectable agglomerates are produced, regardless the amount of GO-COOH used in the synthesis process. Further, the SEM images of bicomponent AGS or GO-COOH-decorated hybrid HAGS-0.1, HAGS-0.2 structures highlight the same regular, well-defined and continuous nanofibrous morphology with no obvious differences, except the presence of carboxylated graphene oxide layers along the hybrid nanofibers (Fig. 1).

### 3.3 Structural characterization

The comprehensive structural characterization of raw materials and all mono/bicomponent standard or GO-COOH-decorated hybrid scaffolds with nanofibrous architecture before and after the crosslinking process was achieved by FTIR spectrometry (Fig. 2a–d).

The FTIR spectra of raw materials are highlighted in Fig. 2a. Firstly, it is worth mentioning the signals from  $\sim 3375\text{ cm}^{-1}$  and  $1242\text{ cm}^{-1}$  registered in the FTIR spectrum of pristine GO-COOH, characteristic to the stretching vibrations of O–H and phenolic C–O bonds, proving that beside COOH, OH functionalities are also presented on the surface of the carboxylated graphene oxide layers.<sup>42,43</sup>

Secondly, the carboxylic functionalities are shown by the typical C=O and C–O stretching vibrations at  $1720\text{ cm}^{-1}$  and  $1050\text{ cm}^{-1}$ .<sup>42</sup> while the signal at  $1586\text{ cm}^{-1}$  is ascribed to the stretching vibration of aromatic rings from the graphene structure.

The gelatin FTIR spectrum discloses the specific peaks of protein secondary structure, *e.g.*, the stretching vibration of N–H bonds from amide A and B at  $3292\text{ cm}^{-1}$  and  $3065\text{ cm}^{-1}$ ; the stretching vibration of C=O from amide I at  $1647\text{ cm}^{-1}$ ; amide II is represented by the out-of-phase combination of the N–H in plane bend and the C–N stretching vibration at  $1540\text{ cm}^{-1}$ ; and amide III is characterized by the in-phase combination of the N–H bending and the C–N stretching vibration at  $1246\text{ cm}^{-1}$ .<sup>44</sup> The FTIR spectrum of sodium alginate reveals the typical peaks of polysaccharide structure *e.g.*, the

broad peak at  $3350\text{ cm}^{-1}$  from the stretching vibration of O–H bonds, the two bands at  $1607\text{ cm}^{-1}$  and  $1410\text{ cm}^{-1}$  represent the asymmetric and symmetric stretching vibration of the COOH group and the peaks at  $1090\text{ cm}^{-1}$  and  $1035\text{ cm}^{-1}$  attributed to C–O–C and C–O stretching vibration, respectively.<sup>45</sup> PEO shows in FTIR the fundamental signals specific to its polyether structure: C–H stretching and bending vibrations of CH<sub>2</sub> groups at  $2885\text{ cm}^{-1}$ ,  $1470\text{ cm}^{-1}$  and  $1344\text{ cm}^{-1}$ ; the symmetric stretching vibration of C–O–C triplet linkage as well as C–C bonds from the polyether backbone chains at  $1105\text{ cm}^{-1}$  and  $957\text{ cm}^{-1}$ , respectively.<sup>46</sup>

Fig. 2b reveals the FTIR spectra of all gelatin-based electrospun uncrosslinked/crosslinked scaffolds. The preservation of polypeptide secondary structure after the electrospinning process is proven by identifying all characteristic spectral bands at approximately the same wavenumber in the FTIR spectra of gelatin-based scaffold with respect to the raw gelatin spectrum. The crosslinking reaction of protein-based scaffolds in the presence of GA vapor is accomplished by the formation of new imine bond (C=N) at  $1645\text{ cm}^{-1}$ , which mostly involves the interaction of aldehyde groups with NH<sub>2</sub> groups of arginine and glutamic acid from fish gelatin through a nucleophilic mechanism; the signal being overlapped by the specific amide I peak (Fig. 2b). Moreover, the GA can also interact with OH functionalities from both protein and GO-COOH structure (according to FTIR spectrum of raw GO-COOH) generating new C–O–C bonds, which appear in the FTIR at  $1030\text{ cm}^{-1}$ .

The FTIR spectra of electrospun alginate-based scaffolds (Fig. 2c) show the typical bands of both pristine sodium alginate and PEO. An additional vibrational band at  $1739\text{ cm}^{-1}$  can be observed in the samples containing GO-COOH (HAS and HAS', the band is more intense at 0.2 wt% GO-COOH content). The band, characteristic to COOH stretching from GO-COOH structure, is shifted to higher wavenumber (from  $1720$  to  $1739\text{ cm}^{-1}$ ) as a result of intermolecular H-bonds that appear between oxygen containing groups of alginate chains and GO-COOH layers.<sup>47</sup> The ionic gelation of sodium alginate-based scaffolds in the presence of Ca<sup>2+</sup> is proven by the shift of asymmetric COOH stretching vibration from  $1410\text{ cm}^{-1}$  to  $1431\text{ cm}^{-1}$  and is correlated with the replacement of Na<sup>+</sup> in the uronic acid by Ca<sup>2+</sup> which determines a modification of charge density owing to the change of the cation atomic weight radius.<sup>48</sup> Moreover, the obvious increase in intensity of OH bands at  $3350\text{ cm}^{-1}$  in the AS', HAS'-0.1 and HAS'-0.2 spectra signifies the involvement of multiple OH groups in the Ca<sup>2+</sup>-mediated gelation process of alginate macromolecules and the formation of characteristic egg-box structure.<sup>26</sup> Beside polysaccharide chains, GO-COOH can also be involved in the gelation process and egg-box formation through synergistic interactions of Ca<sup>2+</sup> ions with the oxygen containing functionalities, mainly the carboxylic groups.<sup>47,49</sup>

The FTIR spectrum of bicomponent AGS electrospun scaffolds (Fig. 2d) is characterized by a prominent absorption band at  $1645\text{ cm}^{-1}$  resulting from the combination of typical protein's amide I band from  $1647\text{ cm}^{-1}$  with the asymmetric stretching vibration of polysaccharide COOH band from  $1607\text{ cm}^{-1}$ . This shift implies the formation of numerous

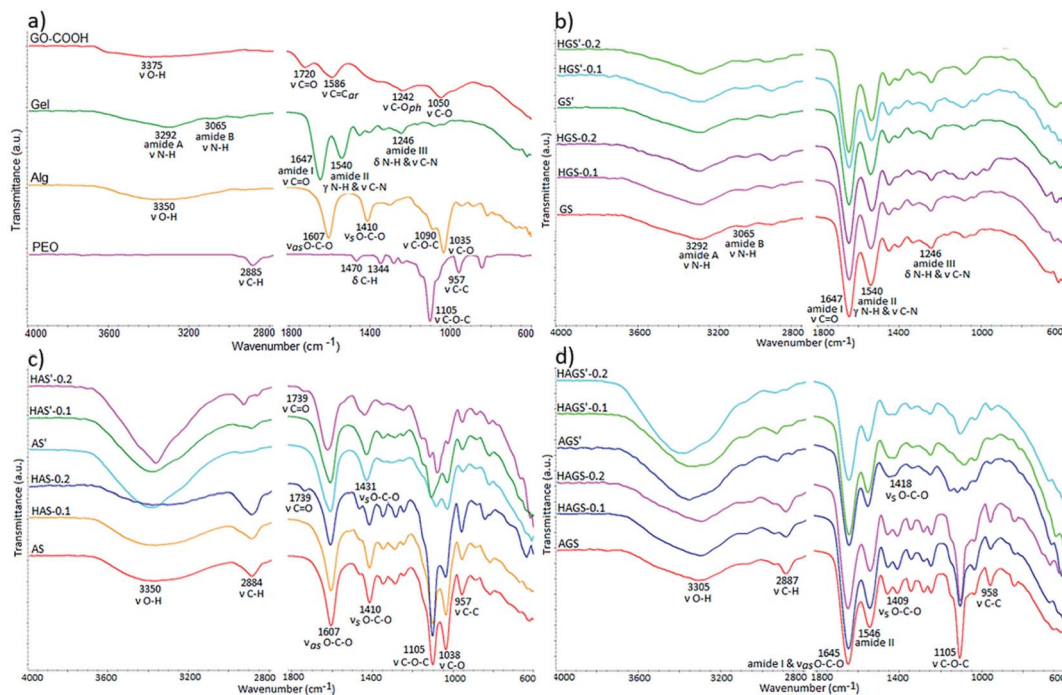


Fig. 2 FT-IR spectra of raw materials – (a), and all investigated uncrosslinked and crosslinked electrospun mono/bicomponent or GO-COOH-decorated biomaterials based on Gel – (b); Alg – (c); and Alg-Gel – (d).

intermolecular interactions including electrostatic and H-bonds between macromolecular chains of biopolymers.<sup>50</sup> The interpenetrated networks of bicomponent hybrid electrospun scaffolds show in FTIR spectra the typical signals of alginate gelation in the presence of  $\text{Ca}^{2+}$  and crosslinked polypeptide chains with GA vapor.

The dispersion of GO-COOH into the mono/bicomponent polymer matrix consequently the development of GO-COOH-decorated hybrid scaffold with nanofibrous architecture is difficult to demonstrate using FTIR analysis since the important signals from GO-COOH are of low intensity or are overlapped with the signals from polymers structure. Therefore, to prove the GO-COOH distribution into the polymer matrix and to study more detailed their structure, the samples were subjected to complementary RAMAN and XPS investigations.

Raman spectrometry is a widely used method in characterization of various type of graphene-based materials, enabling a comprehensive evaluation of important features related to graphene phase such as bonding type, electronic structure, or chemical reactivity as well the orientation of the dispersed graphene layers (*e.g.*, the Bernal or no-Bernal (misoriented) stacking configuration), important parameters that governs the global performances of a material.<sup>24</sup> In this context, Raman investigations on GO-COOH-decorated hybrid scaffolds, pristine GO-COOH and GO-COOH/TX-100 (GO-COOH ultrasonicated for 1 hour in the presence of 0.5 wt% Triton X-100) were performed and the recorded spectra are presented in Fig. 3.

The Raman spectrum of GO-COOH is characterized by two typical strong 1st order bands with obviously discrepancy in

intensity, one at  $\sim 1357 \text{ cm}^{-1}$  and another at  $\sim 1585 \text{ cm}^{-1}$ , which are correlated with D and G-bands position.<sup>51</sup> The D-band is owed to the out-of-plan vibrations associated to the presence of structural disorder or defects while the G-band is assigned to the graphitic structure, implying the in-plan vibration of  $\text{sp}^2$  bonded carbon atoms,<sup>52</sup> which is consistent with FTIR investigations (the C=C bond vibration from graphene planar structure arises in FTIR at  $1586 \text{ cm}^{-1}$ ). Several observations can be made regarding the bands position and relative intensity when comparing the Raman spectrum of pristine GO-COOH with those of GO-COOH/TX-100 and GO-COOH-decorated hybrid nanofibrous scaffolds. Firstly, it is noted a frequency shift of strong G-band toward high wavenumber; this shift has been reported in the literature and is correlated with the number of graphene layers subjected to Raman study.<sup>53</sup> Graf<sup>54</sup> and Kudin<sup>55</sup> have observed this Raman blue shift of G-peak in graphene-

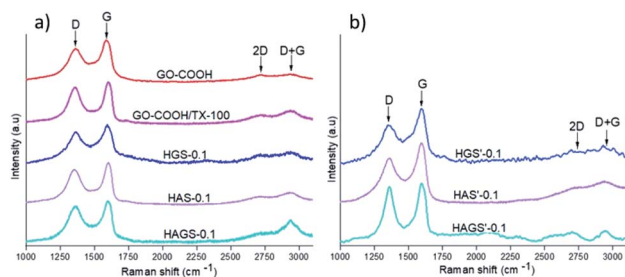


Fig. 3 Raman spectra of GO-COOH, GO-COOH/TX and uncrosslinked – (a) and crosslinked – (b) hybrid nanofibrous samples with 0.1 wt% GO-COOH.

based materials when the multilayer-graphene was replaced with the single graphene sheet. In other words, the number of graphene layers was lowered (at the crossover to the double and especially to the single-layer graphene) in which the isolated C=C bonds resonate at higher frequencies. Considering that, we suppose that this blue shift of G-band might be correlated with the quite exfoliated state of GO-COOH lattices within the hybrid materials. Indeed, this inference can also be sustained by the calculation of  $I_D/I_G$  intensity ratios that are usually applied to obtain quantitative information about the defect density in graphene induced by physical or chemical processes involved in the exfoliation, respectively manufacturing step of scaffolds (Table 3).

As expected, the intermolecular interactions between the GO-COOH and surfactant along with some structural defects in the GO-COOH lattice, considerably increase the  $I_D/I_G$  ratio of GO-COOH/TX as compared to pristine GO-COOH. Actually, the main role of Triton X-100 is to improve the dispersity and stability of GO-COOH lattices within the aqueous media by reducing their van der Waals or  $\pi$ - $\pi^*$  stacking interactions, respectively their tendency to agglomerate. Further on, the same increasing trend in the  $I_D/I_G$  ratio can be observed when an amount of 0.1 wt% GO-COOH was dispersed within the uncrosslinked mono/bicomponent hybrid nanofibrous HGS-0.1, HAS-0.1 and HAGS-0.1 scaffolds. Since the GO-COOH is characterized by a very high chemical activity originated from the presence of oxygen functionalities (as it was confirmed in FTIR analysis) and defects generated during the exfoliation process, this trend might suggest: firstly, the occurrence of numerous interactions (*e.g.*, hydrogen bonding) between the functionalities of polymers chains and GO-COOH (as it was also observed in DLS investigations) and secondly, an increased degree of disordered of graphene through the formation of more  $sp^3$  bonds in defective lattices,<sup>24</sup> both increasing the exfoliation state of GO-COOH, especially in the HAGS-0.1 scaffolds (the  $I_D/I_G$  ratio is 0.95 and the blue shift of G-band to  $1602\text{ cm}^{-1}$ ). In addition, it must be noted that the 2nd order D + G band at  $2937\text{ cm}^{-1}$  is also presented (especially in the HAGS-0.1 spectrum), supporting the presence of graphene sheets in a high exfoliated state within the hybrid matrices.<sup>24,53</sup>

**Table 3** The  $I_D/I_G$  ratios of GO-COOH, GO-COOH/TX and all uncrosslinked and crosslinked hybrid nanofibrous samples with 0.1 wt% GO-COOH from Raman investigations

Sample	D ( $\text{cm}^{-1}$ )	G ( $\text{cm}^{-1}$ )	$I_D/I_G$ (473 nm <sup>a</sup> )
GO-COOH	1357	1585	0.79
GO-COOH/TX	1357	1602	0.88
HGS-0.1	1358	1598	0.83
HAS-0.1	1357	1602	0.84
HAGS-0.1	1359	1602	0.95
HGS'-0.1	1355	1589	0.71
HAS'-0.1	1357	1596	0.75
HAGS'-0.1	1359	1599	0.93

<sup>a</sup> The spectra were acquired using a 473 nm laser excitation wavelength.

In the case of crosslinked samples, a decrease of  $I_D/I_G$  ratios accompanied by a slight downshift of D + G band in the Raman spectra of HGS'-0.1 and HAS'-0.1 hybrid scaffolds that may originate from some re-aggregation phenomena of GO-COOH layers during the crosslinking process, can be observed. Different behaviour is noted for HAGS'-0.1 hybrid scaffolds, the crosslinking process did not significantly impact the GO-COOH dispersion, the  $I_D/I_G$  ratio is 0.93 and the D + G band is still presented in a high intensity in the Raman spectrum, suggesting a still high exfoliation of GO-COOH layers. According to FTIR results and reported literature, the two-step crosslinking process, and the creation of interpenetrated networks, in which the GO-COOH functionalities are also involved, might have a contribution to its high exfoliation state.<sup>47,49</sup>

Further on, the surface electronic state and atomic composition of the GO-COOH, GO-COOH/TX-100 and the designed nanofibrous scaffolds were investigated by XPS spectroscopy. The wide-scan survey spectra of GO-COOH and GO-COOH/TX-100 (Fig. 4) highlight the presence of C and O elements in the materials composition as well the increase of C content with the Triton X-100 addition (Table 4).

Additionally, the high-resolution C 1s spectra of both samples are characterized by three intense peaks centered at 284.8, 286.7 and 288.7 eV and are assigned to non-oxide C (C=C and C-C), ether/hydroxyl C (C-O-C/C-OH) and carboxylate C (O-C=O) bonds (Fig. 4). Compared to pristine GO-COOH, the intensity peaks of (C-O-C/OH) and carboxyl carbon (O-C=O) in the GO-COOH/TX-100 spectrum are strengthened and accompanied with the shift of (O-C=O) peak to 287.6 eV following TX-100 modification/addition. Since the intensity peak is directly connected to the number of atoms in a specific chemical state,<sup>56</sup> this may be coordinated with the formation of numerous H-bonds between the functionalities of components during the sonication process.

Next, the wide-scan survey spectra of standard or GO-COOH decorated hybrid nanofibrous scaffolds (Fig. 5 and Table 4) show the presence of all characteristic elements, as follow: C, O and N in the gelatin-based materials; C, O and Na in the uncrosslinked alginate-based materials and the replacement of Na atoms with Ca and Cl following the polysaccharide gelation process (data are not shown); C, O, N, and Na in the surface composition of bicomponent (AGS) scaffolds and the presence of Ca and Cl instead of Na element following the interpenetrated network of AGS' (data are not shown). Overall, as it is normally expected, an increasing trend in C and O (except the

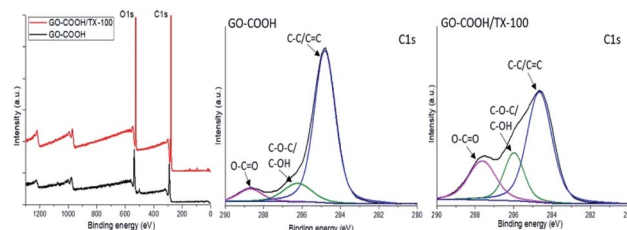


**Fig. 4** Survey and deconvoluted C 1s spectra of GO-COOH and GO-COOH/TX-100.



**Table 4** Atomic surface composition data of GO-COOH, GO-COOH/TX-100 and all uncrosslinked samples obtained from XPS analysis

Sample	C%	O%	N%	Na%
GS	63.82	18.71	17.46	—
HGS-0.1	64.75	19.30	15.34	—
HGS-0.2	66.13	19.87	14.57	—
AS	64.94	32.51	—	2.55
HAS-0.1	65.48	32.21	—	2.32
HAS-0.2	66.23	31.75	—	2.02
AGS	68.00	20.85	10.63	0.51
HAGS-0.1	68.70	21.27	9.41	0.63
HAGS-0.2	70.11	21.53	7.88	0.47
GO-COOH	73.91	26.09	—	—
GO-COOH/TX-100	77.42	22.57	—	—

alginate-based materials) content accompanied by a reduction of N and Na elements with rising the GO-COOH amount in the composition of GO-COOH-decorated hybrid nanofibrous scaffolds, can be observed (Table 4).

Further examinations are accomplished by the deconvolution of XPS spectra. The deconvoluted C 1s spectra of standard uncrosslinked materials and hybrid scaffolds decorated with 0.1 wt% GO-COOH before and after the crosslinking step are presented in Fig. 5.

In the C 1s spectrum of GS, the peaks at binding energies of 283.6, 285.1, 286.9 and 288.5 eV are assigned to C-C/C=C, C-O/C=C=N, C=O/C-N and COOH/O=C-N (hardly observed).<sup>57</sup>

Compared to GS spectrum, a new intense peak at 284.5 eV assigned to  $sp^2$  C-C originating from graphene lattice,<sup>58</sup> as well as a slight strengthens accompanied by the shift of COOH/O=C-N peak to 287.8 eV in the spectrum of HGS-0.1 hybrid nanofibrous scaffolds, can be observed. This shift of 0.7 eV might be ascribed to the occurrence of numerous H-bonds between the functionalities of protein chains and GO-COOH sheets, mainly  $-NH_2$  and  $-COOH$ . Meanwhile, the obvious increase of C=N and/or C-O contents in the case of HGS'-0.1 hybrid nanofibrous structure is generated by the numerous C=N and/or C-O covalent bonds that take place during the protein crosslinking step (consistent to FTIR investigations).

The C 1s deconvoluted spectra recorded for alginate-based nanofibrous materials (AS and HAS-0.1) are characterized by three intense binding energy peaks: 283.4, 284.8 and 286.3 eV being assigned to C-C, C-O and C-O-C/C=O respectively, which are mainly from the chemical structure of polysaccharide, PEO and GO-COOH layers.<sup>59,60</sup> Regarding the HAS'-0.1, the binding energy of the non-oxygenated C-C/C=C is stronger while the C-O peak is substantially weakened following the polysaccharide gelation process. The increase of C-C/C=C peak might be coordinated with the  $\pi$ - $\pi$  stacking interaction of graphene, suggesting the occurrence of some re-aggregation phenomena of GO-COOH layers during the crosslinking process, in agreement with Raman conclusions.

In the C 1s spectra of bicomponent nanofibrous scaffolds (AGS, HAGS-0.1) no significant modifications in the peaks position and intensity characteristic to C-C/C=C, C-O/C=N

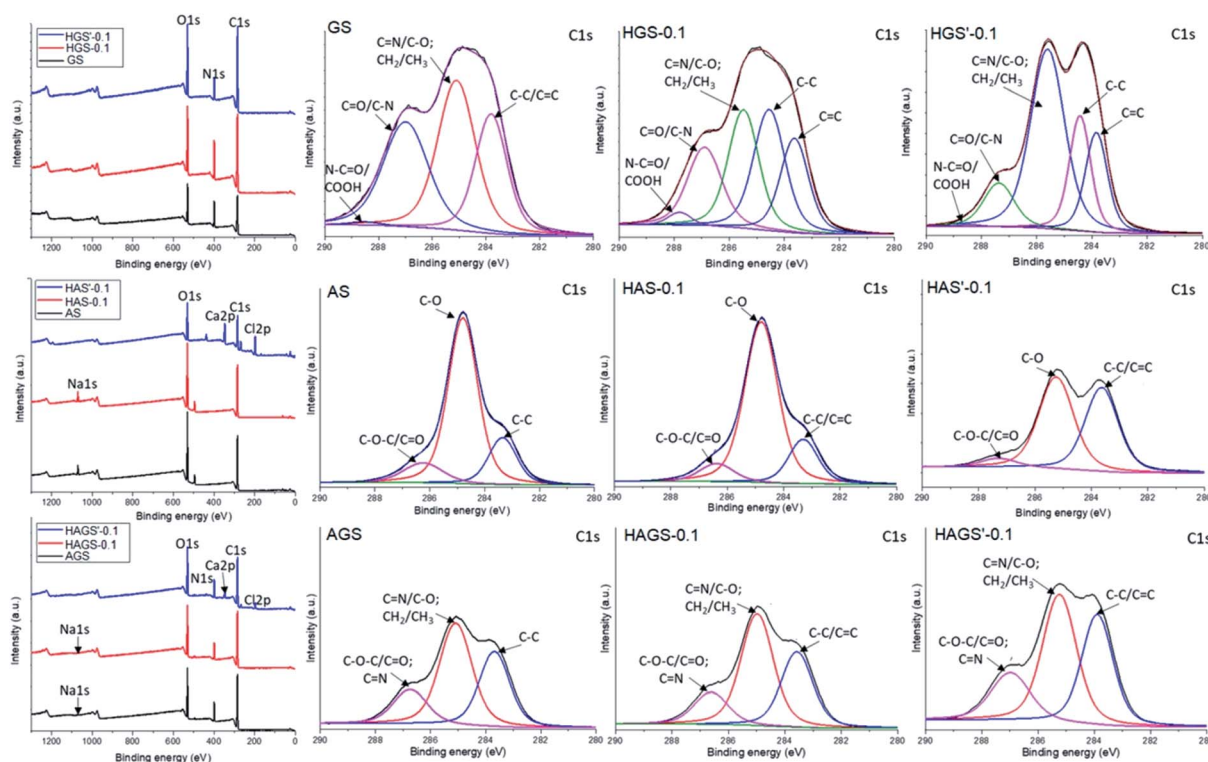


**Fig. 5** Survey and deconvoluted C 1s spectra of mono/bicomponent and 0.1 wt% GO-COOH decorated hybrid scaffolds with nanofibrous architecture.

and C–N/C–O–C/C=O species, are observed. At the same time, in the C 1s spectrum of HAGS'–0.1 a relative high rise of C=N/C–O amount and a slight increase of the non-oxygenated carbon content following the two-step crosslinking process are noted, consistent with FTIR results.

### 3.4 Wettability and water contact angel (WCA)

The wettability property of a scaffold with potential biomedical applications represents one of the critical features that contributes to the achievement of a suitable cell attachment and proliferation to its surface, respectively its integration into the biological environment. The surface hydrophilicity of the crosslinked electrospun mono/bicomponent and GO-COOH-decorated hybrid nanofibrous scaffolds was investigated by measuring their water contact angle (WCA), the obtained results are presented in Fig. 6.

The crosslinked nanofibrous scaffolds based on hydrophilic gelatin, alginate (GS', AS') or their bicomponent counterpart (AGS') present high hydrophilic surfaces with the WCA values in the range of 19.02° to 21.97°. The addition even of low amount of GO-COOH impacts the surface wettability properties of the biomaterials by increasing their WCA values and reducing their affinity to water. According to the obtained results, the values of WCA have an ascending trend with the rise of GO-COOH content. The dispersion of 0.1 wt% GO-COOH increases with ~8% the WCA values of HGS'–0.1, HAS'–0.1 and HAGS'–0.1 hybrid scaffolds, while rising the amount of GO-COOH to 0.2 wt% lead to a substantial growth of WCA value, with ~1.5-folds for HGS'–0.2 (WCA = 32.71°) or HAGS'–0.2 (WCA = 35.14°) and double in the case of HAS'–0.2 hybrid scaffolds (WCA = 41.64°) as compared to their standard counterparts.

It is known that graphene family is characterized by a low affinity to water, regardless of the type of structure and chemical content. The apparent wettability of graphene oxide is driven by its intrinsic wettability (which is merely influenced by the characteristics of pristine graphene and the types of functionalities) and various external factors (*e.g.*, pH value).<sup>61,62</sup> Indeed, besides COOH groups, the hydroxyl functionalities bounded on the graphene surface (observed in the FTIR spectra) not only provide a relevant chemical activity but also define and tune the wetting features of graphene surfaces.<sup>62</sup> Wan *et al.*<sup>63</sup> have demonstrated that graphene oxide film can manifest a hydrophobic character in acidic and neutral water (WCA ~ 135° at pH = 6.0) which became more hydrophilic (WCA ~ 70° at pH =

12.0) when alkaline media are used. The authors claim that the protonation-deprotonation of the surface oxygen-containing functionalities induced by the pH are primarily responsible for the pH-responsive performances of graphene film. Moreover, it is worth noting that the wetting performances of designed nanofibrous biomaterials can be also influenced by the three-dimensional capillary effect of fractal-like structured graphene surface.<sup>64</sup>

### 3.5 Nanomechanical properties

Table 5 summarizes the nanomechanical characteristics of all crosslinked nanofibrous materials determined by nano-indentation technique. It is noted that the nanomechanical properties of materials are highly dependent on the type of chemical reaction involved in the crosslinking process, thus AS' followed ionic gelation registers the lowest Young's modulus ( $E = 0.302$  GPa) when compared to its GS' counterpart ( $E = 0.871$  GPa), which was subjected to a proper chemical crosslinking reaction.

The highest values of nanomechanical features are registered for nanofibrous AGS' scaffolds (*e.g.*,  $E = 3.288$  GPa) and might be correlated with the interpenetrated networks that are generated during the two-step crosslinking reaction. It is interesting to note that the values of mechanical parameters of GO-COOH-decorated hybrid scaffolds with nanofibrous architecture do not outperform those of their standard counterparts, regardless of the type of scaffold; the Young's modulus ( $E$ ), hardness ( $H$ ) and stiffness ( $S$ ) of hybrid materials decrease as GO-COOH loading increases. Although the incorporation of graphene-family members into polymer matrices should generate composite materials with high mechanical characteristics, it is known that the final mechanical performances of these materials are controlled by several parameters related to both polymer matrix and graphene characteristics (*e.g.*, the structure, the dispersion and the interaction of graphene layers within the polymer matrix as well as its orientation).<sup>65</sup>

Therefore, according to the literature, this unusual nanomechanical behaviour of GO-COOH-decorated hybrid materials beyond GO-COOH loading might be correlated with several factors. As previously mentioned, the functional groups of GO-

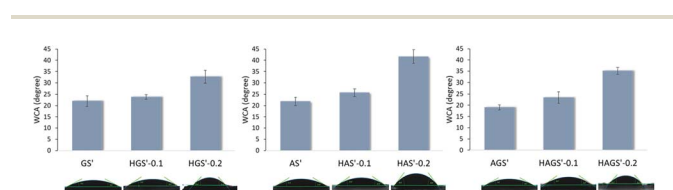


Fig. 6 WCA of all crosslinked electrospun mono/bicomponent and GO-COOH-decorated hybrid nanofibrous scaffolds.

Table 5 The nanomechanical features of all investigated crosslinked scaffolds with nanofibrous architecture<sup>a</sup>

Sample	$E$ (GPa)	$H$ (GPa)	$S$ (N m <sup>-1</sup> )
GS'	0.871	0.080	2521
HGS'–0.1	0.794	0.060	2312
HGS'–0.2	0.545	0.036	1914
AS'	0.302	0.049	598
HAS'–0.1	0.295	0.025	445
HAS'–0.2	0.135	0.021	288
AGS'	3.288	0.646	10 484
HAGS'–0.1	3.022	0.598	8351
HAGS'–0.2	1.403	0.298	4365

<sup>a</sup>  $E$  – Young's modulus,  $H$  – hardness,  $S$  – stiffness, at an indentation depth of 500 nm.

COOH layers can interact with functionalities from gelatin and/or alginate through H-bonding as well as through GA-mediated covalent C–O–C bonds and Ca<sup>2+</sup>-ionic gelation. Firstly, the non-covalent interactions of polymers with GO-COOH might hinder the degree of interaction among various polymer chains involved in the system, increasing their mobility, respectively leading to a reduction in the Young's modulus. Similar effect of GO dispersion on the elastic modulus of electrospun gelatin nanofibers is reported by Jalaja *et al.*<sup>27</sup> Secondly, the covalent bonds created between polymers and GO-COOH can alter the structure of graphene that might impact the global nano-mechanical properties of nanofibrous scaffolds.<sup>66</sup> Then, it is well established that the spatial orientation of the nanofillers within the polymer-based material has a vital role on its collective mechanical properties. The materials with random/misoriented graphene-nanofiller layers present a low Young's modulus as compared to fully aligned ones.<sup>65</sup> The decreasing trend in Young's modulus of hybrid nanofibrous materials with increasing the GO-COOH loading could also be originate from the re-aggregation of GO-COOH layers during the crosslinking, as it was clearly observed in Raman results. It is known that the effective Young's modulus of graphene-based composite materials drops as the number of layers increases. Therefore, the re-aggregation of graphene layers could behave as weak points in the nanofibrous scaffolds weakening the interface properties, respectively their overall mechanical features.<sup>67</sup>

### 3.6 Biocompatibility and proliferation potential

The new designed mono/bicomponent or GO-COOH-decorated hybrid scaffolds with nanofibrous architecture were comparatively investigated for their bioactivity and ability to promote and support the proliferation rate of NCTC fibroblast cells after 2 and 6 days of seeding in standard culture conditions. The quantitative investigations were done by MTT assay using the control sample as reference (Fig. 7).

A visible difference in cellular viability, which may originate from the main manufacturing parameters *e.g.*, scaffold composition and crosslinking step, is registered between the investigated nanofibrous biomaterials and control sample after 2 days of fibroblasts seeding ( $p < 0.05$ ). All investigated biomaterials present a relatively good bioactivity as compared to control sample, except the bicomponent nanofibrous HAGS'-0.1 that shows a remarkable level of fibroblasts viability after 2 days of culture ( $p < 0.05$ ). Significant improvement in cellular metabolic activity, respectively superior proliferation potency is observed on all nanofibrous biomaterials 6 days after fibroblasts incubation, as compared to results registered after 2 days ( $p < 0.0001$ ). An increasing trend in bioactivity and cellular proliferation potency is observed in the case of HAS'-0.1 ( $p < 0.001$ ) and HAGS'-0.1 ( $p < 0.05$ ) while the further increase of GO-COOH content to 0.2 wt% slightly reduces the fibroblasts activity. Considering that the cellular response on graphene-based materials is influenced by both the graphene amount and its intrinsic properties, this might suggest that the addition of 0.1 wt% GO-COOH plays a positive role on cells behaviour and growth, supporting the cells adhesion and proliferation

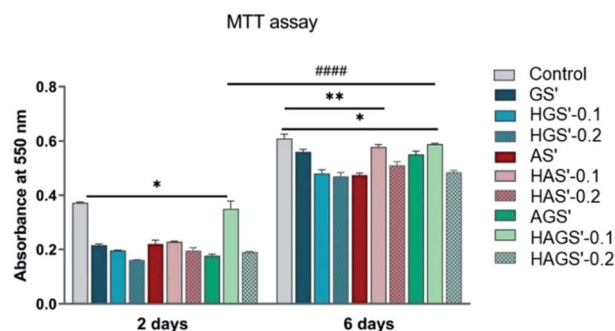


Fig. 7 Viability and proliferation of NTC fibroblasts seeded with nanofibrous scaffolds determined by MTT assay after 2 and 6 days in standard culture conditions. Statistical significance: \* $p < 0.05$ ; \*\* $p < 0.001$  (comparison between two different samples during one time point); #### $p < 0.0001$  (comparison of the same sample between different time points).

while the further rise of GO-COOH amount, through its re-aggregation phenomena that could take place (as it was observed in Raman) may affect/disturb the cells activity by constraining their development.<sup>68</sup> Overall, the highest biocompatibility and proliferation ability is registered for HAGS'-0.1 followed by the HAS'-0.1 hybrid nanofibrous scaffolds.

### 3.7 Cytotoxic assessment

Subsequently, the cytotoxic potential of all designed nanofibrous biomaterials was evaluated by determining the proportion of dead cells indicated by the level of LDH released in the culture media, using as reference the control sample. The obtained results are graphically represented in Fig. 8 and are in full agreement with cellular viability and proliferation results studied by MTT.

According to the registered results all investigated scaffolds with nanofibrous architecture have a reduced cytotoxic effect on the fibroblast cells, the levels of induced toxicity being lower when compared to control samples, regardless the measured time point (after 2 or 6 days). No noteworthy differences in the cytotoxic response of fibroblasts are registered, except the AS' scaffolds that displayed a considerable decrease in cytotoxicity

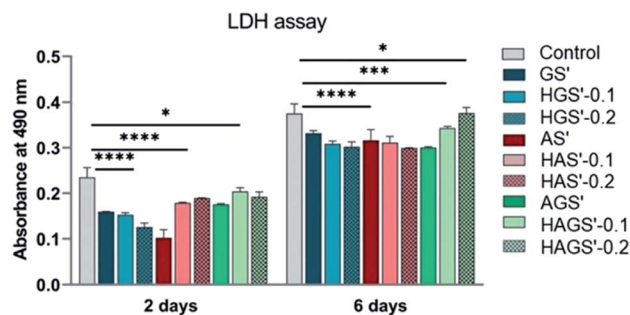


Fig. 8 Cytotoxic response of NTC fibroblasts incubated in the presence of nanofibrous scaffolds measured by LDH assay after 2 and 6 days in standard culture conditions. Statistical significance: \* $p < 0.05$ ; \*\*\* $p < 0.0005$ ; \*\*\*\* $p < 0.0001$ .

after 2 days of culture ( $p < 0.0001$ ). Furthermore, the amount of GO-COOH used in the synthesis process did not significantly influence the cytotoxic profile of hybrid nanofibrous scaffolds ( $p < 0.0001$ ), except for a slight increasing trend in LDH levels with the rise of GO-COOH amount exhibited by HAGS'-0.2 ( $p < 0.05$ ), in accordance with the MTT results. In conclusion, the new designed GO-COOH decorated hybrid scaffolds with nanofibrous architecture display a low cytotoxic potential, which probably is originated from the manufacturing method and/or GO-COOH content and its re-agglomeration phenomena as previously explained.

## 4. Conclusions

In this work we have designed and characterized novel bio-inspired GO-COOH decorated bicomponent hybrid scaffolds with nanofibrous architecture by rationally combining the unique biomimetic and biological characteristics of two biobased-derived polymers, alginate and gelatin with the mechanical and biological features of GO-COOH using electrospinning technique. The GO-COOH decorated bicomponent hybrid scaffolds were subjected to a two-step crosslinking process generating interpenetrated networks, in which the GO-COOH sheets can also be involved through the oxygen containing functionalities presented on their surface as was observed in structural FTIR and XPS investigations. The morphological review (SEM) highlighted the nanometric and uniform fibrous architecture of scaffolds as well the dispersion of graphene layers along the hybrid nanofibers, without forming detectable agglomerates. Nonetheless, the Raman results suggested the occurrence of some re-aggregation phenomena during the crosslinking step, especially in the case of monocomponent hybrid nanofibrous scaffolds. As it was expected, the interpenetrated network of nanofibrous AGS' bicomponent scaffolds led to materials with the highest nanomechanical features (the value of Young's modulus was 10-folds higher as compared to monocomponent counterparts). The increasing trend in elasticity of designed hybrid nanofibrous scaffolds beyond the amount of dispersed GO-COOH might be correlated with the hindering effect of graphene sheets which decreased the extend of interactions among the polymer chains accompanied with some re-aggregation phenomena which occurred during the crosslinking process (in corroboration with Raman investigation). The *in vitro* biological assessments performed on NTC fibroblast highlighted the highest biocompatibility and proliferation ability of HAGS'-0.1 (MTT assay) as well the low cytotoxic potential of GO-COOH decorated hybrid nanofibrous scaffolds (LDH test).

Indeed, there is still an enormous work to be done and beside the physico-chemical and mechanical investigations, the biological concerns remain to be considered. Therefore, our further investigations foresee a comprehensive *in vitro* screening of biological behaviour of the new designed biomaterials to ensure their safety and potency as biomaterials with highly proper features and performances for TERM.

## Conflicts of interest

There are no conflicts to declare.

## Acknowledgements

This work was supported by a grant of the Ministry of Research and Innovation, CNCS-UEFISCDI, project number PN-III-P1-1.1-PD-2019-0205 (contract no. PD 83/2020), within PNCDI III and by the Operational Program Human Capital of the Ministry of European Funds through the Financial Agreement 51668/09.07.2019, SMIS code 124705. The use of electrospinning, DLS, Zeta potential, contact angle and nanoindentation techniques was possible due to European Regional Development Fund through Competitiveness Operational Program 2014–2020, Priority axis 1, ID P\_36\_611, MySMIS code 107066, INOVABIOMED.

## References

- 1 T. Gonzalez-Fernandez, D. J. Kelly and F. J. O'Brien, *Adv. Ther.*, 2018, **1**, 1800038.
- 2 N. Bhattarai, Z. Li, D. Edmondson and M. Zhang, *Adv. Mater.*, 2006, **18**, 1463–1467.
- 3 T. C. Mokhena and A. S. Luyt, *Carbohydr. Polym.*, 2017, **165**, 304–312.
- 4 T. Jiang, E. J. Carbone, K. W.-H. Lo and C. T. Laurencin, *Prog. Polym. Sci.*, 2015, **46**, 1–24.
- 5 M. Norouzi, S. M. Boroujeni, N. Omidvarkordshouli and M. Soleimani, *Adv. Healthcare Mater.*, 2015, **4**, 1114–1133.
- 6 S.-B. Park, E. Lih, K.-S. Park, Y. K. Joung and D. K. Han, *Prog. Polym. Sci.*, 2017, **68**, 77–105.
- 7 R. P. Babu, K. O'Connor and R. Seeram, *Prog. Biomater.*, 2013, **2**, 8.
- 8 S. Kumar, Sarita, M. Nehra, N. Dilbaghi, K. Tankeshwar and K.-H. Kim, *Prog. Polym. Sci.*, 2018, **80**, 1–38.
- 9 L. Gu, T. Shan, Y.-X. Ma, F. R. Tay and L. Niu, *Trends Biotechnol.*, 2019, **37**, 464–491.
- 10 P. Sobhanian, M. Khorram, S.-S. Hashemi and A. Mohammadi, *Int. J. Biol. Macromol.*, 2019, **130**, 977–987.
- 11 M. A. Pattison, S. Wurster, T. J. Webster and K. M. Haberstroh, *Biomaterials*, 2005, **26**, 2491–2500.
- 12 C. A. Bonino, K. Efimenko, S. I. Jeong, M. D. Krebs, E. Alsberg and S. A. Khan, *Small*, 2012, **8**, 1928–1936.
- 13 J. K. Y. Lee, N. Chen, S. Peng, L. Li, L. Tian, N. Thakor and S. Ramakrishna, *Prog. Polym. Sci.*, 2018, **86**, 40–84.
- 14 S. Ramakrishna, K. Fujihara, W.-E. Teo, T. Yong, Z. Ma and R. Ramaseshan, *Mater. Today*, 2006, **9**, 40–50.
- 15 I. P. S. Fernando, W. W. Lee, E. J. Han and G. Ahn, *Chem. Eng. J.*, 2019, **391**, 123823.
- 16 R. M. D. Soares, N. M. Siqueira, M. P. Prabhakaram and S. Ramakrishna, *Mater. Sci. Eng., C*, 2018, **92**, 969–982.
- 17 C. D. Saquing, C. Tang, B. Monian, C. A. Bonino, J. L. Manasco, E. Alsberg and S. A. Khan, *Ind. Eng. Chem. Res.*, 2013, **52**, 8692–8704.
- 18 C.-C. Wang, K.-C. Yang, K.-H. Lin, Y.-L. Liu, H.-C. Liu and F.-H. Lin, *Biomaterials*, 2012, **33**, 120–127.

- 19 K. Y. Lee and D. J. Mooney, *Prog. Polym. Sci.*, 2012, **37**, 106–126.
- 20 K. Su and C. Wang, *Biotechnol. Lett.*, 2015, **37**, 2139–2145.
- 21 N. Davidenko, C. F. Schuster, D. V. Bax, R. W. Farndale, S. Hamaia, S. M. Best and R. E. Cameron, *J. Mater. Sci.: Mater. Med.*, 2016, **27**, 148.
- 22 V. M. Merkle, L. Zeng, M. J. Slepian and X. Wu, *Biopolymers*, 2014, **101**, 336–346.
- 23 H. W. Kwak, M. Shin, J. Y. Lee, H. Yun, D. W. Song, Y. Yang, B.-S. Shin, Y. H. Park and K. H. Lee, *Int. J. Biol. Macromol.*, 2017, **102**, 1092–1103.
- 24 D. G. Papageorgiou, I. A. Kinloch and R. J. Young, *Prog. Mater. Sci.*, 2017, **90**, 75–127.
- 25 D. P. Singh, C. E. Herrera, B. Singh, S. Singh, R. K. Singh and R. Kumar, *Mater. Sci. Eng., C*, 2018, **86**, 173–197.
- 26 Y. He, N. Zhang, Q. Gong, H. Qiu, W. Wang, Y. Liu and J. Gao, *Carbohydr. Polym.*, 2012, **88**, 1100–1108.
- 27 K. Jalaja, V. S. Sreehari, P. R. A. Kumar and R. J. Nirmala, *Mater. Sci. Eng., C*, 2016, **64**, 11–19.
- 28 Y. Ma, P. Qi, J. Ju, Q. Wang, L. Hao, R. Wang, K. Sui and Y. Tan, *Composites, Part B*, 2019, **162**, 671–677.
- 29 S. S. Majidi, P. Slemming-Adamsen, M. Hanif, Z. Zhang, Z. Wang and M. Chen, *Int. J. Biol. Macromol.*, 2018, **118**, 1648–1654.
- 30 Y. Dror, W. Salalha, R. L. Khalfin, Y. Cohen, A. L. Yarin and E. Zussman, *Langmuir*, 2003, **19**, 7012–7020.
- 31 Y. Ding, W. Li, F. Zhang, Z. Liu, N. Zanjanzadeh Ezazi, D. Liu and H. A. Santos, *Adv. Funct. Mater.*, 2019, **29**, 1802852.
- 32 W.-W. Hu, Y.-C. Wu and Z.-C. Hu, *Carbohydr. Polym.*, 2018, **183**, 29–36.
- 33 M. Bera, Chandravati, P. Gupta and P. K. Maji, *J. Nanosci. Nanotechnol.*, 2018, **18**, 902–912.
- 34 D. Cho, S. Lee and M. W. Frey, *J. Colloid Interface Sci.*, 2012, **372**, 252–260.
- 35 S. M. Ahsan and C. M. Rao, *Int. J. Nanomed.*, 2017, **12**, 795–808.
- 36 N. Okutan, P. Terzi and F. Altay, *Food Hydrocolloids*, 2014, **39**, 19–26.
- 37 M. Doi, S. F. Edwards and S. F. Edwards, *The theory of polymer dynamics*, Oxford University Press Inc., New York, 1988.
- 38 E. Olaret, J. Ghitman, H. Iovu, A. Serafim and I.-C. Stancu, *Polym. Adv. Technol.*, 2020, **31**, 645–653.
- 39 J. Stetefeld, S. A. McKenna and T. R. Patel, *Biophys. Rev.*, 2016, **8**, 409–427.
- 40 A. Kyzioł, J. Michna, I. Moreno, E. Gamez and S. Irusta, *Eur. Polym. J.*, 2017, **96**, 350–360.
- 41 S. Ramazani and M. Karimi, *Polym. Compos.*, 2016, **37**, 131–140.
- 42 S. Yu, J. Liu, W. Zhu, Z.-T. Hu, T.-T. Lim and X. Yan, *Sci. Rep.*, 2015, **5**, 16369.
- 43 I. Biru, C. M. Damian, S. A. Gârea and H. Iovu, *Eur. Polym. J.*, 2016, **83**, 244–255.
- 44 A. Barth, *Biochim. Biophys. Acta, Bioenerg.*, 2007, **1767**, 1073–1101.
- 45 B. Sarker, D. G. Papageorgiou, R. Silva, T. Zehnder, F. Gul-E-Noor, M. Bertmer, J. Kaschta, K. Chrissafis, R. Detsch and A. R. Boccaccini, *J. Mater. Chem. B*, 2014, **2**, 1470–1482.
- 46 L. H. Sim, S. N. Gan, C. H. Chan and R. Yahya, *Spectrochim. Acta, Part A*, 2010, **76**, 287–292.
- 47 R. Sabater i Serra, J. Molina-Mateo, C. Torregrosa-Cabanilles, A. Andrio-Balado, J. M. Meseguer Dueñas and Á. Serrano-Aroca, *Polymers*, 2020, **12**, 702.
- 48 W.-P. Voo, B.-B. Lee, A. Idris, A. Islam, B.-T. Tey and E.-S. Chan, *RSC Adv.*, 2015, **5**, 36687–36695.
- 49 S. Park, K.-S. Lee, G. Bozoklu, W. Cai, S. T. Nguyen and R. S. Ruoff, *ACS Nano*, 2008, **2**, 572–578.
- 50 S. R. Derkach, N. G. Voron'ko, N. I. Sokolan, D. S. Kolotova and Y. A. Kuchina, *J. Dispersion Sci. Technol.*, 2019, **41**, 690–698.
- 51 W. Su, N. Kumar, A. Krayev and M. Chaigneau, *Nat. Commun.*, 2018, **9**, 1–7.
- 52 Y. Li, J. Li, Y. Li, Y. Li, Y. Song, S. Niu and N. Li, *Ultrason. Sonochem.*, 2018, **40**, 798–807.
- 53 A. Gupta, G. Chen, P. Joshi, S. Tadigadapa and P. C. Eklund, *Nano Lett.*, 2006, **6**, 2667–2673.
- 54 D. Graf, F. Molitor, K. Ensslin, C. Stampfer, A. Jungen, C. Hierold and L. Wirtz, *Nano Lett.*, 2007, **7**, 238–242.
- 55 K. N. Kudin, B. Ozbas, H. C. Schniepp, R. K. Prud'Homme, I. A. Aksay and R. Car, *Nano Lett.*, 2008, **8**, 36–41.
- 56 A. V. Naumkin, A. Kraut-Vass, S. W. Gaarenstroom and C. J. Powell, *NIST X-ray photoelectron spectroscopy database, NIST standard reference database 20, version 4.1*. US Department of Commerce, Washington, 2012.
- 57 M. Qi, Y. Zhou, Y. Huang, L. Zhu, X. Xu, Z. Ren and J. Bai, *Nanoscale*, 2017, **9**, 637–646.
- 58 Y. Zhuang, F. Yu, H. Chen, J. Zheng, J. Ma and J. Chen, *J. Mater. Chem. A*, 2016, **4**, 10885–10892.
- 59 Z. Tong, Y. Chen, Y. Liu, L. Tong, J. Chu, K. Xiao, Z. Zhou, W. Dong and X. Chu, *Mar. Drugs*, 2017, **15**, 91.
- 60 Q. Huang, S. Liu, K. Li, I. Hussain, F. Yao and G. Fu, *J. Mater. Sci. Technol.*, 2017, **33**, 821–826.
- 61 L. A. Belyaeva and G. F. Schneider, *Surf. Sci. Rep.*, 2020, **75**, 100482.
- 62 J. Feng and Z. Guo, *Nanoscale Horiz.*, 2019, **4**, 339–364.
- 63 S. Wan, J. Pu, X. Zhang, L. Wang and Q. Xue, *Appl. Phys. Lett.*, 2013, **102**, 011603.
- 64 G. McHale, N. J. Shirtcliffe, S. Aqil, C. C. Perry and M. I. Newton, *Phys. Rev. Lett.*, 2004, **93**, 036102.
- 65 Z. Li, R. J. Young, N. R. Wilson, I. A. Kinloch, C. Vallés and Z. Li, *Compos. Sci. Technol.*, 2016, **123**, 125–133.
- 66 P. H. Shah and R. C. Batra, *Comput. Mater. Sci.*, 2014, **95**, 637–650.
- 67 M. A. Ashraf, W. Peng, Y. Zare and K. Y. Rhee, *Nanoscale Res. Lett.*, 2018, **13**, 214.
- 68 M. Pelin, L. Fusco, V. León, C. Martín, A. Criado, S. Sosa, E. Vázquez, A. Tubaro and M. Prato, *Sci. Rep.*, 2017, **7**, 40572.